ARTICLE

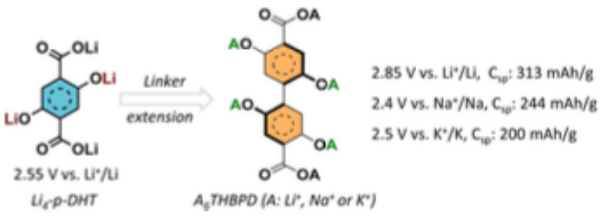

A hexaanionic carboxyphenolate framework for high energy alkali cation storage

Vasudeva Rao Bakuru, Petru Apostol, Darsi Rambabu, Shubhadeep Pal, Xiaodong Lin, Robert Markowski, Tom Goossens, Da Tie, Andrii Kachmar, Yan Zhang, Géraldine Chanteux and Alexandru Vlad*

The development of high-performance alkali-rich organic positive electrode materials remains a significant challenge.

Energy & Environmental Science

ROYAL SOCIETY OF CHEMISTRY

PAPER

A hexaanionic carboxyphenolate framework for high energy alkali cation storage†

Cite this: DOI: 10.1039/d4ee05701e

Vasudeva Rao Bakuru, Petru Apostol, Darsi Rambabu, Shubhadeep Pal, Xiaodong Lin, Robert Markowski, Tom Goossens, Da Tie, Andrii Kachmar, Yan Zhang, Géraldine Chanteux and Alexandru Vlad *

DOI : 10.1039/D4EE05701E

A Hexaanionic Carboxyphenolate Framework for High Energy Alkali Cation Storage

Vasudeva Rao Bakuru,[a] Petru Apostol,[a] Darsi Rambabu,[a] Shubhadeep Pal,[a] Xiaodong Lin,[a] Robert Markowski,[a] Tom Goossens,[a] Da Tie,[a] Andrii Kachmar,[a] Yan Zhang,[a] Géraldine Chanteux,[a] and Alexandru Vlad*[a]

The development of high-performance alkali-rich organic positive electrode materials remains a significant challenge. Recent advances across various classes of organic compounds have led the achievement of either high capacity or high voltage improvements. However, the quest for materials that simultaneously offer both high capacity and voltage, and thus high-energy density remains challenging. Herein, we report a new organic redox system, 2,2',5,5'-tetrahydroxy-4,4'-biphenyl dicarboxylic acid (H_6THBPD), designed for high-performance alkali metal-ion storage. The prepared Li_6, Na_6, and K_6THBPD positive electrodes reveal a high degree of redox utilization, with nearly four electrons ($4e^-$) per formula unit attained, resulting in specific capacities of 313, 244, and 200 mAh/g, for Li-, Na-, and K-ion storage, respectively. A high redox potential of 2.85 V vs. Li^+/Li, 2.4 V vs. Na^+/Na, and 2.5 V vs. K^+/K is observed, attributed to the combined electron-withdrawing effect, and reduced conjugation, which destabilize charge localization and thereby increase the redox potential. These metrics position the developed A_6THBPD phases among the best in alkali containing form positive electrode materials reported to date. A prototype Li-ion full-cell using a graphite anode is assembled and shown to provide an output voltage of 2.7 V, with competitive cycling performances. This study expands the potential applications of monovalent cations in conjugated carboxyphenolate organic chemistry.

Introduction

Developing renewable energy storage materials to improve the performance of next-generation batteries remains a critical challenge in sustainable electrochemical storage technologies area. Organic redox-active materials have emerged as promising alternatives to inorganic battery components, which face increasing scarcity due to limited terrestrial availability.[1,2] These materials represent a promising choice for future electrochemical energy storage applications, thanks to their inherent abundance of constituent elements, sustainability, and reduced environmental impact in potential future production and recycling processes.[3] Additionally, organic materials offer advantages due to their exceptional compositional diversity and structural flexibility, enabling synthetic control for the tailored design of positive electrode materials. This adaptability makes them suitable not only for Li-ion storage, but also other alkali metal ions, extending their applicability to multivalent cation systems.[4,5] However, despite recent progress, organic batteries still exhibit low gravimetric and volumetric energy metrcis when compared to the mature inorganic counterparts. Beyond Li-ion storage, emerging technologies now employ a variety of post-Li metal cations (e.g., Na^+, K^+, Mg^{2+}, Ca^{2+}, Zn^{2+}, and even Al^{3+}) as active species in electrode materials.[6, 7] Integrating these cations with organic molecules is essential, as post-Li batteries represent a promising approach toward improving the sustainability of next-generation energy storage systems.[8] Such systems could potentially address some of the limitations of conventional lithium-ion technology.

Recent efforts have led to the development of alkali-ion-containing organic positive electrode materials across various chemistries, including oximates,[9] sulfonamides,[10–12] cyanamides and triflimides,[13] as well as the probably the most studied to date enolate-carbonyl materials.[14-24] Given that it is the first chemistry to be tested for battery applications,[25,26] considerable work has been devoted in the recent years to increasing the redox potential of the parent Li-diphenolate center (**Scheme 1**), achieving advancements through electron-withdrawing or donating substituents,[17,18] stereoelectronic effects,[22] sacrificial metal-mediated charge delocalization,[23] and the polymorphism of dilithium(2,5-dilithium-oxy)-terephthalate (Li_4-*o*-DHT, β-phase).[14] For example, Renault *et al.* made notable advancements by using the lithium salt of dihydroxy terephthalic acid (Li_4-*p*-DHT) as redox-active component, achieving excellent stability up to 80 cycles at an average potential of 2.55 V vs. Li^+/Li.[19] Furthermore, Wang *et al*. demonstrated that Li_4-*p*-DHT nanosheets exhibited a high capacity with an average potential of 2.6 V vs. Li^+/Li.[20] Compared to Li_4-*p*-DHT, the α-phase of Li_4-*o*-DHT was found to operate at a higher potential (2.85 V vs. Li^+/Li), attributed to a stereoelectronic effect. These developments are considered seminal in the field of Li-ion containing organic phases for battery applications, despite the fact that the studied phases remain unstable to ambient air exposure and triggered further research into developing materials with intrinsic high voltage and air-stability.

Considering the above, numerous efforts over the past years have focused on increasing the working potential of the enol-quinone redox center, employing various approaches. For example, a new β-phase of Li_4-*o*-DHT was found to operate at 250 mV higher potential (3.1 V vs. Li^+/Li) as compared to the α-phase, phenomenon explained by a polymorphism-induced effect.[14] Sieuw *et al*. reported the tetra-lithium salt of 2,5-dihydroxy-1,4-benzenediacetate (Li_4-*p*-DOBDA), which demonstrated an unusually high redox potential of 3.35 V vs. Li^+/Li in the solid phase, a 650 mV enhancement relative to the liquid state (2.70 V vs. Li^+/Li), attributed to stereoelectronic effect.[22] The spectator cation effect has also been

[a] *Institute of Condensed Matter and Nanosciences, Molecular Chemistry, Materials and Catalysis, Université catholique de Louvain, Louvain-la-Neuve B-1348, Belgium. E-mail: alexandru.vlad@uclouvain.be*

demonstrated as an effective strategy to modulate the redox potential of organic positive electrode material. For carboxy-phenolates (M[Li_2]-*p*-DHT), the incorporation of Mg^{2+} ions resulted in a reversible lithium intercalation/de-intercalation potential of up to 3.4 V (vs. Li^+/Li) for the Mg(Li_2)-*p*-DHT phase, representing a 900 mV increase compared to the parent Li_4-*p*-DHT material. The high polarizing power of Mg^{2+} ions regulated the density of p-electrons, inducing electron deficiency on phenolates through the inductive effect (-I).[23] In a similar context, Rambabu *et al*. demonstrated that lithiated magnesium- and manganese-based metal-organic frameworks (Li_2-Mg/Mn-*p*-DHT MOFs) exhibit an average potential of approximately 3.2 V vs. Li^+/Li. The Li_2-Mn-*p*-DHT MOF, in particular, displayed good reversibility, retaining 91% of its initial capacity after 100 cycles. It is worth noting that Li_2-Mn-*p*-DHT[24] is structurally similar to that of Mg(Li_2)-*p*-DHT[23], while Li_2-Mg-*p*-DHT[24] adopts a distinct polymorph. These findings suggest that both the nature of the spectator cation and polymorphism play significant roles in tuning the average potential.[24]

Although considerable progress has been achieved in organic Li-ion storage materials (**Table S2**), as illustrated by the examples above, research on Na-ion and K-ion containing organic positive electrodes remains limited, with only a few examples reported to date (**Table S3**). For instance, Na_4-*p*-DHT as a positive electrode, displayed an average potential of 2.3 V vs. Na^+/Na, and enabled the construction of a symmetrical all-organic rocking chair cell with an average operating voltage of 1.8 V.[21] More recently, Wang *et al*. investigated a new series of alkali-ion containing benzene-1,2,4,5-tetrayltetrakis methylsulfonylamide tetra-anionic ligand (Na_2/K_2-PTtSA)[11] and their corresponding coordinated polymers (Na_2/K_2-Co-PTtSA). The Na_2-Co-PTtSA and K_2-Co-PTtSA positive electrodes exhibited the highest redox potentials reported to date for Na- and K-ion batteries, delivering values of 2.93 V vs. Na^+/Na and 3.25 V vs. K^+/K, respectively.[12] Although different cations (Li^+, Na^+, K^+) influence energy storage and redox potential, there is limited research on their impacts using the same positive electrode material. This necessitates an evaluation of the structural composition and variations within the diphenolate backbone. Furthermore, extending the *p*-DHT framework to

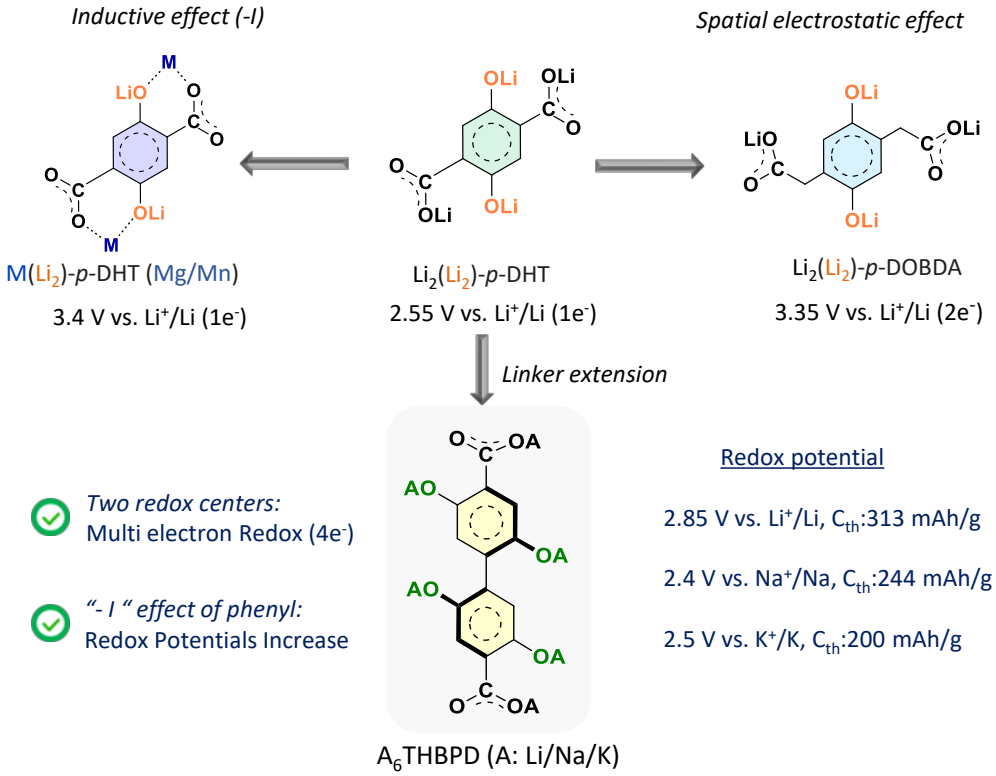

Scheme 1. The design of the high-capacity A_6THBPD positive electrode material, relying on similar functional advances for Li-carboxy-phenolate positive electrodes for organic-based battery systems. Compared to traditional redox systems, the A_6THBPD system has a lower molar mass (Mw= 306 g/mol, for Li_6THBPD) per redox equivalent (four electrons, 4e$^-$) resulting thus in a high capacity, requiring just one carboxylate (COO^-) group per quinone rather than two as compared to the -p-DHT counterpart.

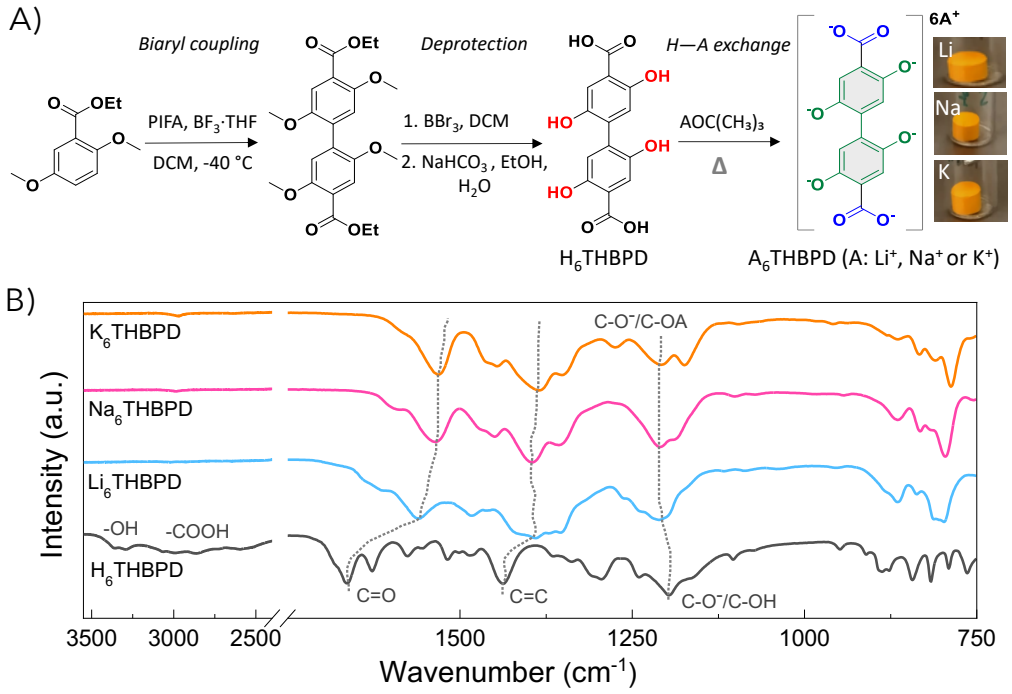

Figure 1. A) The synthetic pathway developed for the preparation of H_6THBPD and A_6THBPD (A: Li^+, Na^+, or K^+) electrode materials. B) Fourier Transform Infrared (FTIR) spectra highlighting characteristic bands and comparing H_6THBPD to A_6THBPD (A: Li^+, Na^+, or K^+) phases.

incorporate a biphenyl system could[27] enhance both capacity and redox potential, owing to the presence of two redox centers, with the electron-withdrawing (-I) effect of the phenyl groups mutually influence and stabilize each other through resonance. In the salt forms of A_6THBPD (where A = Li, Na, or K), steric repulsion between the ortho-OA substituents hinders full conjugation (some degree of conjugation is still maintained due to the inherent symmetry of the molecule), leading to destabilized charge delocalization and raise of the redox potentials (**Scheme 1**).

In this work, we leverage the advantages of a multi-redox system to expand the library of alkali-ion-conjugated carboxyphenolates as positive electrode materials for organic batteries by introducing a new organic redox-active material, the 2,2',5,5'-tetrahydroxy-4,4'-biphenyl dicarboxylic acid (H_6THBPD, **Scheme 1**). Structurally, this system can be viewed as a dimer of the *p*-DHT framework; however, it features only a single carboxylate (COO^-) group per redox center, unlike *p*-DHT, which has two carboxylate groups per redox center. This modification reduces the molar mass (198 g/mol per $2e^-$ *vs*. 306 g/mol per $4e^-$) and increases the theoretical specific capacity by 23% (313 mAh/g *vs*. 242 mAh/g for the lithiated phases). The conversion of the hexa-protonated ligand to the hexa-anionic metal salt is further studied, requiring a unique synthesis approach due to the high charge density attained through progressive deprotonation. Our strategy employs a solvent-free, dry approach that relies on alkali tert-butoxides and the formation of volatile reaction products. This drives the equilibrium towards alkali metal salt formation by effectively removing tert-butanol as a byproduct in an eco-friendly manner. The resulting Li_6THBPD, Na_6THBPD, and K_6THBPD positive electrode materials show reversible four-electron ($4e^-$) redox behavior, centered on two redox quinone units, achieving high specific charge capacities of 313 mAh/g, 244 mAh/g, and 200 mAh/g, respectively, positioning these materials among the leading candidates for alkali metal ion storage (**Tables S2** & **S3**). Cycling analyses with controlled limited capacity indicate that the intrinsic solubility of oxidized intermediates affects the performance, with stable cycling achieved for lower material utilization. Ex-situ infrared spectroscopy and dQ/dV analysis revealed that the redox mechanism of Li_6THBPD follows a two-step, two-electron redox process involving tetra-enolate (Li_6THBPD) ↔ di-quinonoid (Li_4THBPD) ↔ di-quinone (Li_2THBPD) phases transition. A full-cell prototype, consisting of Li_6THBPD as the positive electrode and graphite as the negative electrode, delivers an output voltage of 2.7 V, demonstrating competitive cycling performance. Overall, this study broadens the scope of alkali-ion organic positive electrode materials and enhances our understanding of enol-quinone redox chemistry, contributing to the development of next-generation energy storage technologies.

Results and discussion

The synthesis of 2,2',5,5'-tetrahydroxy-4,4'-biphenyl dicarboxylic acid (H_6THBPD) involves three main steps: an oxidative biaryl coupling reaction,[28] followed by two deprotection steps (1 & 2),[29, 30] as outlined in **Figure 1A** (for details refer to Supplementary Information). The synthesized

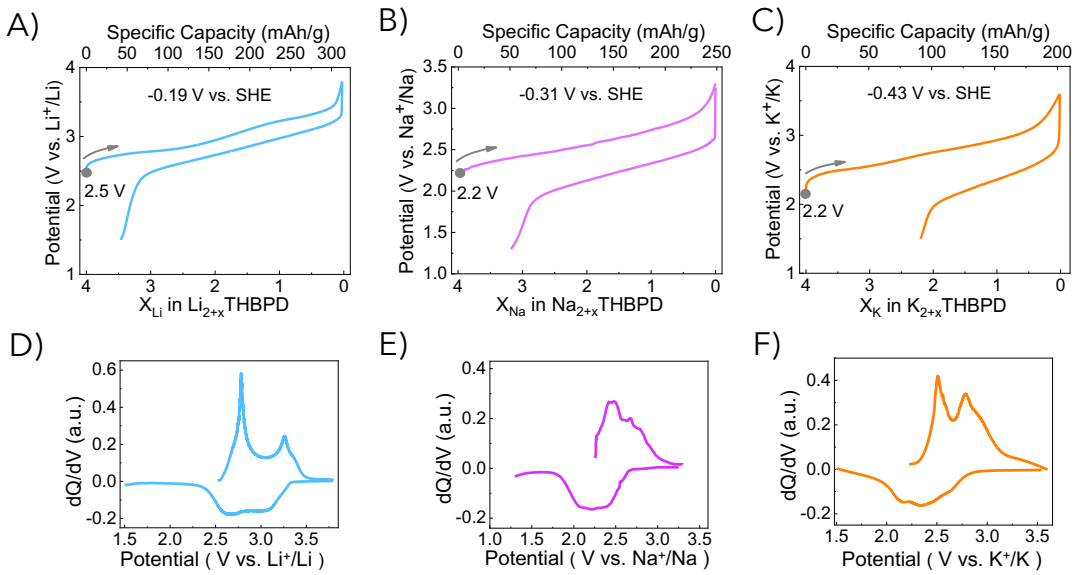

Figure 2. Galvanostatic charge-discharge profiles obtained at a rate of 0.1C (4A$^+$ exchanged in 10 hours, 1C corresponding to 313 mA/g, 244 mA/g, 200 mA/g) for A) Li_6THBPD electrode in 1M $LiPF_6$ in EC/DMC electrolyte; B) Na_6THBPD electrode in 3M NaTFSI in diglyme electrolyte, and C) K_6THBPD electrode in 1M KTFSI in EC/DEC electrolyte, with the associated dQ/dV plots shown in panels D), E), and F). Two electrode metal-cell configurations were assembled and used here. The typical mass loading for the working electrode was of 5 mg per cell of active material (50 wt%), mixed with 40 wt% Super-P carbon and 10 wt% poly(tetrafluoroethylene) (PTFE) as the binder.

H_6THBPD was extensively characterized, confirming the composition, structure and purity (**Figure 1B**, **Figures S5, S6** & **S7**). A distinctive feature of H_6THBPD is the presence of two hydrobenzoquinone redox centers, which contribute to a lower molecular weight compared to *p*-DHT (198.02 g/mol per 2e$^-$ vs. 306.04 g/mol per 4e$^-$).[31-34] These redox centers enable multi-electron activity accompanied by alkali cations exchange (Li^+/Na^+/K^+). Additionally, the carboxylate groups support the anionic nature of the ligand by coordinating with alkali cations, forming coordination frameworks that help mitigate potential solubility issues. To achieve proton exchange, and considering the hexaanionic nature of H_6THBPD, a strong base (pKa > 14) was required. This was initially attempted using lithium methoxide in methanol at room temperature under an inert atmosphere. However, this approach was unsuccessful, resulting in partially lithiated products (H_{6-x}/Li_xTHBPD). This failure can be attributed to the polyanionic nature of the ligand, where each deprotonation step increases the pKa value of the remaining protons, eventually surpassing the pKa of the reactant alkali base used (*e.g.*, methoxide, pKa of 16).

To address this issue, proton exchange was carried out by reacting H_6THBPD with stoichiometric amounts of alkali metal tert-butoxides (t-BuOH, pKa = 17) under solid-state mechano-chemical conditions, followed by thermal treatment under reduced pressure (refer to Supplementary Information for details). The resulting volatile by-product, tert-butanol, was evacuated under vacuum and heat treatment, displacing the equilibrium towards the formation of A_6THBPD (A: Li^+, Na^+ or K^+) salt. This resulted in the formation of orange colored A_6THBPD solids, as shown in **Figure 1A**. A key advantage of this approach is the solvent-free formation of the hexa-anionic salt, which significantly reduces the E-factor of the process (refer to supporting information in Section 5), making it highly eco-friendly.[19]

Full deprotonation was confirmed by Fourier-transform infrared spectroscopy (FTIR) analysis, which showed the complete disappearance of the characteristic hydroxy bands (ν_{O-H}, phenolic, 3250-3420 cm^{-1}, and ν_{O-H}, carboxylic acid, 3100-2700 cm^{-1}), along with a shift in the carbonyl ($\nu_{C=O}$) band from 1663 cm^{-1} to lower wavenumbers (1545±15 cm^{-1}) due to coordination with alkali ions (**Figure 1B**).[22] A shift in the phenolate group band from 1195 cm^{-1} (ν_{C-O}/δ_{C-O-H}) to 1216-1208 cm^{-1} further supports the proton-cation exchange.[22-24] The powder X-ray diffraction (PXRD) patterns of the metal salts (A_6THBPD) differ from that of H_6THBPD, with the low-angle peak at 5.5° (2θ) in H_6THBPD shifting to 4.5° (2θ) in Li_6THBPD. This change can be attributed to the enlarged unit cell resulting from the coordination of Li with the linker, thereby corroborating the formation of Li_6THBPD (**Figure S7A**). The PXRD patterns indicate a poor crystalline nature for lithium (Li) salts, transitioning to amorphous states for sodium (Na) and potassium (K) salts, indicative of short-range crystalline order. This poor crystallinity order may facilitate ease of cation insertion and removal during electrochemical discharge and charge cycles, as certain amorphous coordination polymers and compounds have been shown to demonstrate enhanced performance under such conditions.[9, 11, 12] Scanning electron microscopy (SEM) analysis (**Figures S7B, C, D** & **E**) reveals that H_6THBPD forms well-defined, elongated crystallites with smooth surfaces. Li_6THBPD (**Figure S7C**) and Na_6THBPD (**Figure S7D**) exhibit morphologies broadly similar to H_6THBPD, but with less-defined, partially fragmented plate-like particles, suggesting a moderate loss of structural coherence upon deprotonation. In contrast, K_6THBPD (**Figure S7E**) presents a distinctly different morphology,

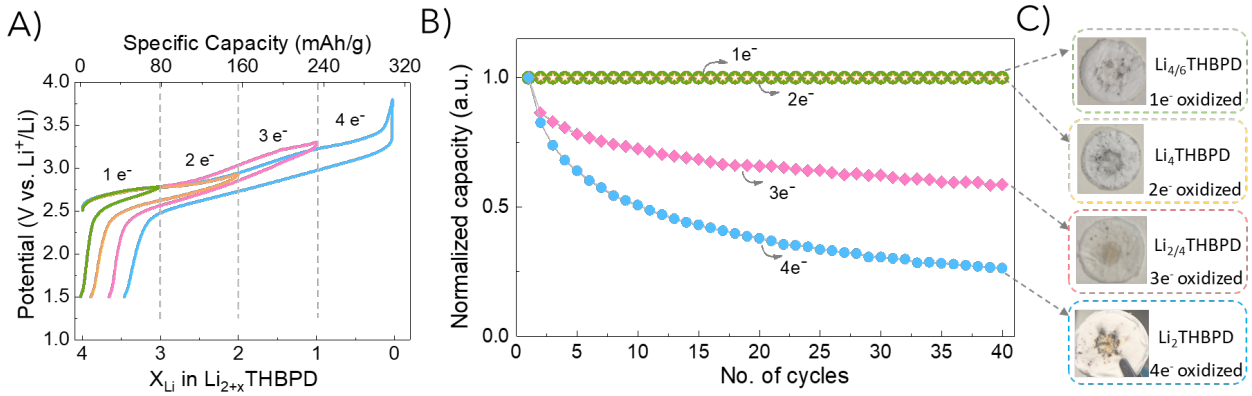

Figure 3. A) First cycle galvanostatic charge-discharge profiles of Li_6THBPD positive electrode material at a rate of 0.1C, and with limited capacity cycling (1 to 4e$^-$, corresponding to 78 mAh/g, 156 mAh/g, 234 mAh/g, and 313 mAh/g). B) The corresponding normalized discharge capacity over 40 cycles for each capacity limit. C) Visual inspection photographs of the separators for the cycled cells.

consisting of densely packed spherical aggregates lacking discernible crystalline features. The composition of the synthesized A_6THBPD materials were confirmed through elemental analysis (carbon and hydrogen) and inductively coupled plasma optical emission spectroscopy (ICP-OES) for metal content, with results consistent with theoretical values (**Table S1**). In addition, the A_6THBPD phases stability was assessed upon exposure to ambient air for a duration of 24h. The Li_6THBPD phase exhibited mainly sensitivity to moisture (as confirmed by FTIR analysis, **Figures S8A** & **D**), whereas the Na_6THBPD and K_6THBPD materials underwent partial oxidation under similar conditions (**Figures S8B, C** & **D**).[19] As next discussed in **Figure 2**, Na_6THBPD and K_6THBPD have a redox potential of 2.40 V and 2.50 V vs. Na^+/Na and K^+/K, while Li_6THBPD has 2.85 V vs. Li^+/Li. Consequently, Na_6THBPD and K_6THBPD are more prone to oxidation by ambient molecular oxygen because of lower redox potentials.[9, 13] This can be explained by the higher polarizing power of contained cations following the series - $Li^+ > Na^+ > K^+$.[11] This indicates that the redox potential plays a role in ambient stability, and that counter cations influencing this potential may affect air sensitivity in related materials.

Electrochemistry and Charge Storage Properties

After confirming the structural and compositional characteristics of the synthesized materials, we investigated their electrochemical charge storage performance. The galvanostatic charge-discharge profiles of A_6THBPD materials (**Figure 2**) revealed average redox potentials of 2.85 V *vs.* Li^+/Li, 2.40 V *vs.* Na^+/Na and 2.50 V *vs.* K^+/K, for the respective compositions. To facilitate a clear comparison, the average redox potentials of Li_6THBPD, Na_6THBPD, and K_6THBPD are also referenced against the standard hydrogen electrode (SHE), corresponding to -0.19 V, -0.31 V, and -0.43 V, respectively. **Figure 2** illustrates a clear trend in which an increasing electron density at the $THBPD^{6-}$ redox center correlates with a decrease in redox potential. This effect is attributed to the reduced polarizing power of the alkali cations (*e.g.* $Li^+ > Na^+ > K^+$).[11] Interestingly, Li_6THBPD exhibits a potential increase of 300 mV (2.85 V vs. 2.55 V) compared to its monomeric analogue Li_4-*p*-DHT.[19] This enhancement can be attributed to the biphenyl system, where the reciprocal electron-withdrawing (-I) effects[17] of the phenyl groups influence each other, but also given the reduced conjugation (non-planar system), with resulting destabilized charge (de)localization, thus raising the redox potential.

Galvanostatic cycling of Li_6THBPD within a potential window of 1.5 to 3.8 V vs. Li^+/Li at a rate of 0.1 C resulted in a specific charge capacity of 313 mAh/g (close to theoretical value), corresponding to the extraction of four lithium ions ($4Li^+$) and four electrons ($4e^-$). The process was found to be reversible up to 3.5e$^-$, with a first-cycle coulombic efficiency of 87.6% (**Figures 2A** & **2D**). Comparable electrochemical performance was observed for the Na_6THBPD and K_6THBPD analogues, exhibiting high specific capacities of 244 mAh/g for Na_6THBPD and 200 mAh/g for K_6THBPD. However, the reversible capacities were found of only 3.1 electrons and 2.1 electrons at the first discharge step (**Figures 2B** & **2C**). The derivative plots (dQ/dV) of A_6THBPD displayed two sets of redox peaks, suggesting a two-step, two-electron redox process (**Figure 2D, 2E** & **2F**, *vide infra*). Although A_6THBPD achieved full theoretical charge capacities, the capacity retention upon full material utilization was unsatisfactory as shown in **Figure S12**. Furthermore, ex-situ SEM analysis (**Figure S13**) at different states of charge (SOCs) supports this observation. For instance, the pristine electrode (**Figure S13B**) displays an irregular and fragmented composite with a relatively smooth surface, characteristic of the as-synthesized material. At 50% SOC (**Figure S13C**), slight surface roughening and emerging microstructural changes become evident, suggesting the onset of electrochemical reactions. Upon full charge (**Figure S13D**), the electrode exhibits more pronounced morphological changes, including increased surface roughness and textural variations, which may be associated with degradation, solubility of the oxidized phase, or structural transformations occurring during complete lithium extraction. These changes contribute to poor cycling stability under full Li extraction conditions. For organic battery

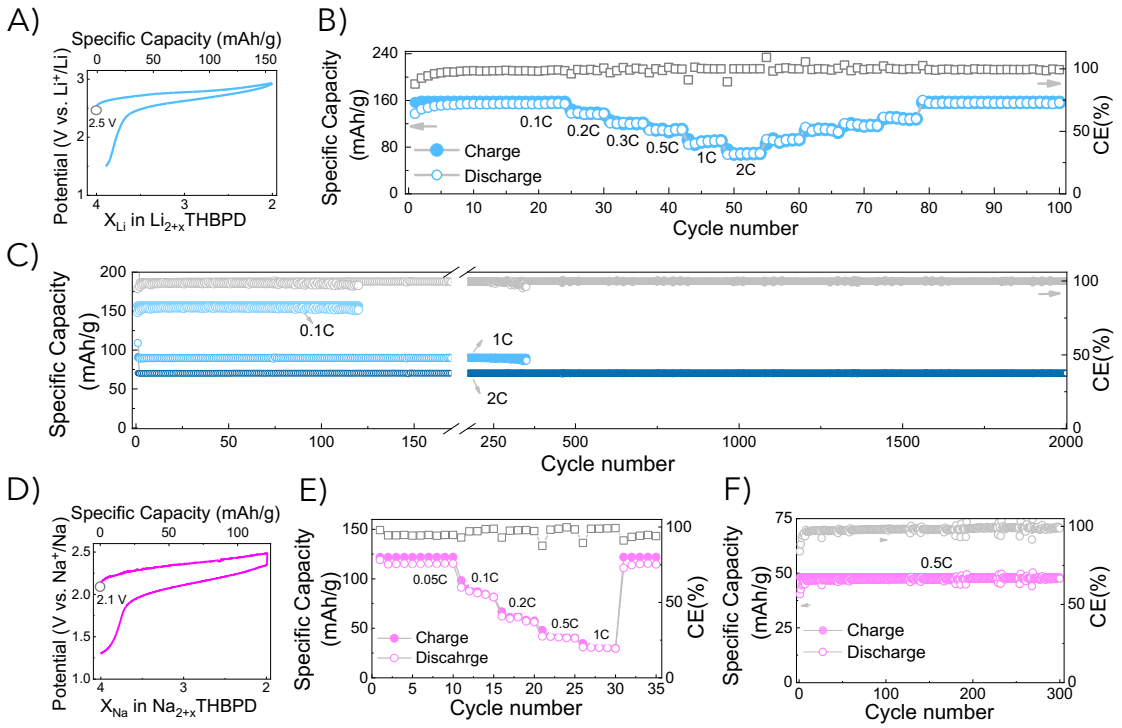

Figure 4: A) Galvanostatic charge-discharge profiles for the $Li_6THBPD|Li$ cell obtained at 0.1C current rate in 1M $LiPF_6$ in EC/DMC electrolyte. B) The cycling stability along with the capacity–rate test for Li_6THBPD electrode. C) Long-term cycle stability for the Li_6THBPD at different charge-discharge rates (0.1C, 1C, and 2C). D) The galvanostatic charge-discharge profile of $Na_6THBPD|Na$ using a 3M NaTFSI in diglyme and cycled at a rate of 0.05C. E) Capacity–rate test for Na_6THBPD and F) Capacity retention during the long-term cycling for the Na_6THBPD positive electrode at rate of 0.5C.

materials, two primary factors likely contribute to this performance: (i) limited anodic stability and potential degradation of the material due to intrinsic instability of the oxidized phase, especially at the high voltages required in this context; or (ii) solubility issues, where either the pristine material or its intermediate and final oxidized species dissolve, leading to elution of active material species from the electrode. However, as discussed further, the four-electron ($4e^-$) oxidized phase was found to be stable, isolated and characterizable, thus ruling out the first hypothesis.

Further investigation of the Li_6THBPD positive electrode material was conducted to understand the factors contributing to capacity fading, with a focus on examining the solubility during cycling with various limited capacities. Although pristine Li_6THBPD was found insoluble in most solvents and conventional electrolytes (**Figures S9, S10** & **S11**), attention shifted to a qualitative assessment of oxidized species. To evaluate this, cells with similar construction, mass loading, and electrolyte amounts were tested over 40 cycles with capacity limits set based on the number of electrons extracted (**Figure 3**). A slow rate of 0.1C was deliberately selected since the solubility and elution effects are time sensitive, thus slow cycling (nearly 24 hours for one full cycle), evidencing this. The galvanostatic charge-discharge profiles for different degrees of material utilization show reversible behavior, and low polarization, with the primary distinction being the reduced coulombic efficiency at higher material utilization (**Figure 3A**). The normalized cycling stability data for $3e^-$ (noted as $Li_{2/4}THBPD$ – yet this being a mixture of Li_2THBDP and Li_4THBDP, 50:50%, as discussed next in the mechanism redox analysis) and $4e^-$ (Li_2THBPD) limited capacity cycling demonstrated capacity loss over cycles, due to the solubility of fully oxidized products, as indicated by the coloration on the glass fibers separator (**Figures 3B** & **C**).[32] A similar phenomenon was observed in Na_6THBPD and K_6THBPD analogues, which exhibited comparable capacity loss and separator staining under analogous electrochemical conditions (**Figure S14**), supporting a dissolution-driven degradation mechanism.

In contrast, limiting cycling to $2e^-$ and $1e^-$ capacity exhibited stable performance, with 98.6% and 99.9% capacity retention after 40 cycles, respectively, without any coloration of the separator (**Figures 3B** & **S18**). This resilience is likely attributed to the fortification of the intermolecular network between anions and Li^+ cations ($Li_6THBPD \leftrightarrow Li_4THBPD$), rendering the dissolution of positive electrode significantly more challenging at any given stage. For $3e^-$ and $4e^-$ extraction processes, the noticeable capacity decay is attributed to the solubility of the partially oxidized ($Li_{2/4}THBPD$) and fully oxidized (quinone form of Li_2THBPD) species in the electrolyte. [32, 34] This interpretation is supported by the complete solubility of chemically oxidized Li_2THBPD in the electrolyte, as confirmed by experimental observations (**Figure S17**). While various approaches have been proposed in the literature to mitigate the solubility of intermediate organic redox species, [32, 34] such strategies fall outside the scope of this initial development work, where our focus remains on stable cycling at practical levels of material

utilization. Although the achieved capacity is approximately 50% of the theoretical maximum, this proof-of-concept phase confirms the applicability of Li_6THBPD as a positive electrode material.

Due to the low electronic conductivity of organic electrode materials, [1,9] initial optimization efforts focused on adjusting the carbon content (**Figure S19**), which was varied from 40 wt.% down to 10 wt.% Super-P carbon. Increasing active material while reducing Super-P lowers conductivity and increases polarization, impacting cycling stability. In contrast, as shown in **Figure S19B,** increasing carbon content effectively reduces polarization and enhances cycling stability (**Figures 4B** & **4C).** Rate capability tests from 0.1C to 2C (**Figure 4B**) reveal that Li_6THBPD retains 44% of its capacity at 1C rate, with a stable coulombic efficiency throughout. Reducing the rate to 0.1C restores the initial capacity, suggesting that the observed capacity losses are due to kinetic limitations rather than degradation. Li_6THBPD electrode material also demonstrates excellent stability, with capacity retention of 99% at a rate of 0.1 C (**Figure 4C**). This performance is one of the best achieved for an organic lithium positive electrode (**Table S2**). The enhanced stability can be attributed to a strengthened intermolecular network between anions and Li^+ ions (Li_6THBPD ↔ Li_4THBPD), which further impedes electrode dissolution throughout the two-electron ($2e^-$) redox process.

The Li_6THBPD also demonstrates favorable rate capability, delivering a capacity of 92 mAh/g (60% of the theoretical capacity) at a 1C rate and 72 mAh/g (48% of the theoretical capacity) at a 2C rate. At these rates, capacity retention of 90 mAh/g and 70 mAh/g are maintained after 350 and 2000 cycles respectively, with high average coulombic efficiencies of 99.6% and 99.4% (**Figure 4C**). Similar results were obtained for the

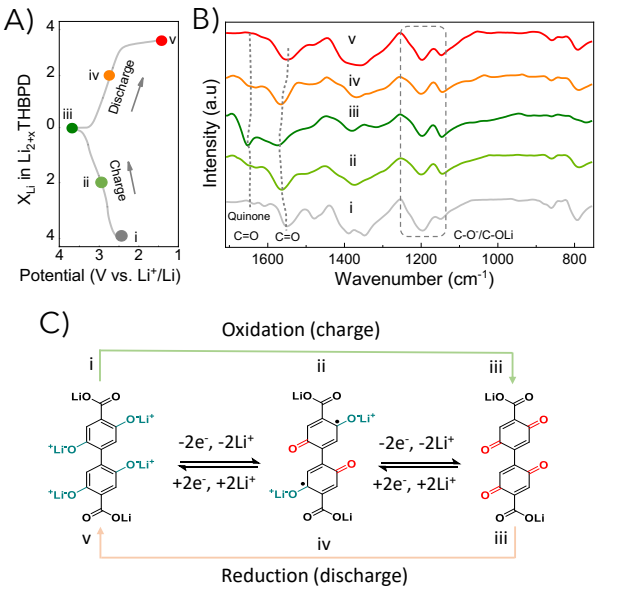

Figure 5: A) Voltage-composition profile at a 0.1C rate. B) Ex-situ Infrared Spectroscopy (IR) analysis of electrode composite collected at distinct states: i (pristine), ii (half, $2e^-$ charged), iii (fully, $4e^-$ charged), iv (half, $2e^-$ discharged), and v (fully, $4e^-$ discharged), corresponding to the stages indicated in the voltage-composition profile. C) Proposed reaction intermediates involved in the charge and discharge processes.

sodium-based counterparts, as shown in **Figures 4** (**D, E** & **F**). The Na_6THBPD material achieved a capacity of 122 mAh/g at a rate of 0.05C, with cycling limited to a two-electron ($2e^-$) process (**Figures 4D** & **S20**). Additionally, Na_6THBPD also exhibited favorable rate capabilities (**Figure 4E**) and maintained a capacity of 40 mAh/g (~34% of the theoretical capacity) at a 0.5C rate over 300 cycles (**Figure 4F**). Finally, the K_6THBPD exhibited a capacity of 100 mAh/g ($2e^-$), comparable to that of Li_6THBPD and Na_6THBPD as shown in **Figure S21**. This performance reflects the reversible exchange of $2K^+$ ions per formula unit at a rate of 0.1C. However, the cell efficiency declined rapidly with cycling. Potential contributors to this reduced performance may include the inefficiency of the potassium plating/stripping process, or the instabilities at the potassium metal-electrolyte interface.

Redox Mechanism Analysis

To investigate the redox mechanism of Li_6THBPD in detail, ex-situ infrared spectroscopy (IR) was performed at various charge and discharge states, as depicted in **Figures 5** (**A** & **B**). IR spectra were recorded for distinct states including the pristine composite (Li_6THBPD, Super-P, and PTFE) electrode material (i); half-charged at 3.0 V, or equivalent of $2e^-$ redox (ii); fully charged at 3.8 V, or equivalent of $4e^-$ redox (iii); half-discharged at 2.8 V (iv), and fully discharged at 1.5 V (v). Given the high reversibility of the process (**Figure 2A**), the IR spectra of the fully discharged Li_6THBPD state (v) matches the one of the pristine state (i). In the half-charged (ii) and fully charged (iii) states, the appearance of a quinonoid carbonyl ($\nu_{C=O}$) peak between 1643-1653 cm^{-1} indicates the weakening of the C-O stretching mode in phenolic (ν_{C-O-Li}) groups.[18,20,35] A reversible trend was observed during the half-discharge state (iv), which aligned with the half-charge state (ii), providing insight into the redox activity of the enolate/quinonoid carbonyl pair during cycling. Additionally, the ^{1}H NMR spectra of the chemically oxidized state of Li_2THBPD and Li_6THBPD exhibited characteristic shifts in the aromatic proton signals, with de-shielding from δ 7.36 to 7.43 ppm and shielding from δ 6.85 to 6.75 ppm. These chemical shift changes are attributed to electron withdrawal and the formation of quinonoid structures, consistent with the redox transformation of the enolate/quinonoid carbonyl moiety (**Figures S15** & **S16**). The proposed mechanism in this redox sequence, as also supported by the dQ/dV analysis includes transition from Li_6THBPD (tetra-enolate) to Li_4THBPD (di-quinoid radical, $2e^-$), and finally to Li_2THBPD (di-quinone, $4e^-$), as illustrated in **Figure 5C**. [31-34] Correlation to the dQ/dV data (**Figure 2D)** wherein two sets of redox peaks are visible, supports a sequential two-by-two electron redox process. During the first redox peak (2.78 V vs. Li^+/Li) associated with the extraction of two electrons from Li_6THBPD, the C-O stretching bands characteristic of the quinonoid function group emerge at 1643 cm^{-1}, along with a shift in the asymmetric vibration bands of the carboxylate functional groups from 1551 to 1564 cm^{-1}, as shown in **Figure 5B.** Notably, upon extracting the remaining $2e^-$ (redox peak at 3.27 V, **Figure 2D**), a pronounced shift in the ν_{as} (COO^-) carboxylate band from 1563 cm^{-1} to 1573 cm^{-1} and the

quinone C=O stretching band at 1653 cm^{-1} is observed. Conversely, during discharge, the reverse electrochemical reactions occur at 3.03 V and 2.65 V, resulting in formation successive intermediates. Overall, the ex-situ infrared spectra, dQ/dV plot and the chemical oxidation products analysis corroborate the participation of quinone redox centers in the charge storage mechanism, supporting the most plausible reaction pathway (**Figures 5C, S15** & **S16**) for the Li_6THBPD positive electrode material. In addition to the primary redox center, A_6THBPD may exhibits electrochemical activity at its carboxylate groups. This typically involves the reduction of carboxylate moieties to form alkali enolates, a process that occurs at potentials below 1.0 V, characteristic of anode-type behaviour (**Figure S22**). [36, 37]

Li_6THBPD|Graphite full-cell

Given the good cycling stability results attained (**Figure 4C**), we assembled and tested full-cell prototype to evaluate Li_6THBPD as a positive electrode in a Li-ion cell. Prior to constructing the full cell, the performance of Li_6THBPD positive electrode with high mass loading of 12 mg/cm^2 was tested in a half-cell configuration against Li metal. The initial two cycles were performed at a 0.1C rate (162 mAh/g for $2e^-$), followed by continuous cycling at a 2C rate, demonstrating stable cycling by maintaining 63% of its capacity after 350 cycles (**Figure S23**).

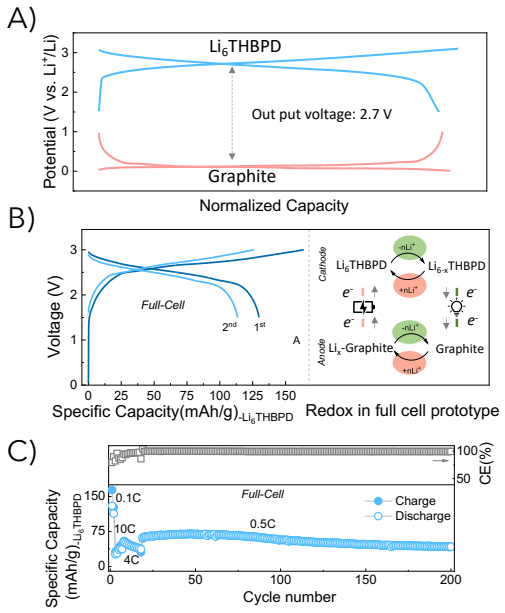

Figure 6. A) Normalized capacity comparison of half-cell tests using Li_6THBPD and graphite against a Li metal counter electrode, with an estimated output voltage of 2.7 V. B) Galvanostatic charge–discharge profiles for the first and second cycles of the full-cell with the Li_6THBPD positive electrode paired with a graphite anode, including a schematic representation of the cell operation. C) Specific capacity retention of Li_6THBPD|graphite full-cell during long cycling.

The comparison of the galvanostatic potential-capacity profiles in half-cell tests for Li_6THBPD and graphite against a Li metal counter electrode suggested to an output voltage of 2.7 V or the full-cell construct (**Figure 6A**). Based on these observations, a full-cell was assembled by integrating the Li_6THBPD positive electrode with the graphite negative electrode, and cycled within the 1.5-3.0 V voltage window[38, 39] (**Figure 6B**). As expected, the average cell voltage was indeed of 2.7 V. The formation of the solid electrolyte interphase (SEI) on the graphite anode likely contributes to the low coulombic efficiency (CE) of approximately 80% in the first cycle, a value consistent with other reported organic systems.[10] The cell was initially cycled at 0.1C, followed by 10C, and 4C, demonstrating the ability to deliver capacity at high rates with good cycling stability at a 0.5C rate, retaining 68% of its capacity over 200 cycles (**Figure 6C**).

Conclusion and outlook

A new hexaanionic organic redox active material capable of supporting a four-electron ($4e^-$) redox is disclosed. The alkali containing materials A_6THBPD (where A = Li, Na, or K) demonstrate high capacity and robust redox activity. Li_6THBPD is found to exhibit a 300 mV higher potential (2.85 V vs. 2.55 V) as compared to the Li_4-*p*-DHT unit, due to the reciprocal electron-withdrawing (-I) effect of the phenyl moieties as well as reduced conjugation, with destabilized charge delocalization. The redox potential trend follows $Li^+ > Na^+ > K^+$ versus SHE (-0.19 V, -0.31 V, and -0.43 V), aligning with the decreasing polarizing power of the alkali cations. The developed Li_6, Na_6, and K_6THBPD positive electrode materials position among the highest-capacity alkali-containing organic positive electrodes, with capacities of 313 mAh/g, 244 mAh/g, and 200 mAh/g for Li-, Na-, and K-ion storage, respectively. Despite capacity limitations due to solubility, the materials demonstrate good electrochemical reversibility upon active material utilization limitation. Ex-situ infrared spectroscopy and dQ/dV analysis, confirm a two-step, two-electron redox process involving enolate/quinone transitions throughout the charge/discharge cycles. A proof-of-concept full-cell prototype using the Li_6THBPD positive electrode delivers an output voltage of 2.7 V, demonstrating its practical applicability. This study broadens the library of alkali-ion organic positive electrode materials and enhances the understanding of alkali-ion chemistry for future energy storage applications.

Author Contributions

B.V.R. and A.V. conceived and designed the project concept. B.V.R. contributed and performed a major part of the experimental work, assisted by P.A., D.R., S.P., X.L., R.M., T.G., D.T., A.K., Y.Z., and G. C. The solid-state method was initially developed by D.R. and subsequently optimized by B.V.R. All authors made iterative contributions and changes to the experiments during implementation and later analysis, working collaboratively as a team. All authors contributed to the scientific discussion of the results as well as participated in the writing and approved the manuscript.

Conflicts of interest

There are no conflicts to declare.

Acknowledgements

This work was supported by FWO and F.R.S.-FNRS under the Excellence of Science (EOS) program - ECOBAT [40007515]; as well as partial support from the European Research Council (ERC) under the European Union's Horizon 2020 research and innovation program (grant agreement No. 770870, MOOiRE). B.V.R., D.R. and X.L acknowledge F.R.S.-FNRS for Chargé de Recherché (CR) fellowship (grant agreement No. 40023657, 40010410 and 40010559). X.L. acknowledges financial support from the Marie Skłodowska-Curie Actions (grant agreement No. 101064286) for his postdoctoral fellowship. D.T. and Y.Z. acknowledge CSC for the PhD fellowships. R.M., T.G and G. C. acknowledge FRS-FNRS for PhD fellowships. We thank the Fonds de la Recherche Scientifique-FNRS (F.R.S.-FNRS) for funding a high-resolution NMR (convention UG00122).

References

1 P. Poizot, J. Gaubicher, S. Renault, L. Dubois, Y. Liang, and Y. Yao, Chem. Rev., 2020, **120**, 6490–6557.

2 J. M. Tarascon, Philos. Trans. R. Soc. A Math. Phys. Eng. Sci., 2010, **368**, 3227–3241.

3 D. Larcher, and J. M. Tarascon, *Nat. Chem.,* 2015, **7**, 19–29.

4 Y. Chen, K. Fan, Y. Gao, and C. Wang, *Adv. Mater.*, 2022, **34**, 1–16.

5 J. Xie, and Q. Zhang, *Small.,* 2019, **15**, 1805061.

6 Y. Liang, H. Dong, D. Aurbach, and Y. Yao, *Nat. Energy*., 2020, **5**, 646–656.

7 Z. Pan, X. Liu, J. Yang, X. Li, Z. Liu, X. J. Loh, and J. Wang, *Adv. Energy Mater.,* 2021, **11**, 1–24.

8 J. Bitenc, K. Pirnat, O. Lužanin, and R. Dominko, *Chem. Mater.,* 2024, **36**, 1025–1040.

9 J. Wang, P. Apostol, D. Rambabu, X. Guo, X. Liu, K. Robeyns, M. Du, Y. Zhang, S. Pal, R. Markowski, F. Lucaccioni, A. E. Lakraychi, C. Morari, J. F. Gohy, D. Gupta, and A. Vlad, *Sci. Adv.*, 2023, **9**, 1–12.

10 J. Wang, A. E. Lakraychi, X. Liu, L. Sieuw, C. Morari, P. Poizot, and A. Vlad, *Nat. Mater.,* 2021, **20**, 665–673.

11 J. Wang, X. Liu, H. Jia, P. Apostol, X. Guo, F. Lucaccioni, X. Zhang, Q. Zhu, C. Morari, J. F. Gohy, and A. Vlad, *ACS Energy Lett.,* 2022, **7**, 668–674.

12 J. Wang, X. Guo, P. Apostol, X. Liu, K. Robeyns, L. Gence, C. Morari, J. F. Gohy, and A. Vlad, *Energy Environ. Sci.,* 2022, **15**, 3923–3932.

13 X. Guo, P. Apostol, X. Zhou, J. Wang, X. Lin, D. Rambabu, M. Du, S. Er, and A. Vlad, *Energy Environ. Sci.*, 2023, **17**, 173–182.

14 L. Bernard, A. Jouhara, E. Quarez, Y. Levieux-Souid, S. Le Caër, P. Tran-Van, S. Renault, and P. Poizot, *Inorganics.,* 2022, **10**, 62.

15 H. Chen, M. Armand, M. Courty, M. Jiang, C. P. Grey, F. Dolhem, J. M. Tarascon, and P. Poizot, *J. Am. Chem. Soc.,* 2009, **131**, 8984–8988.

16 Y. Zhang, J. Wang, P. Apostol, D. Rambabu, A. Eddine Lakraychi, X. Guo, X. Zhang, X. Lin, S. Pal, V. Rao Bakuru, X. Chen, and A. Vlad, *Angew. Chemie - Int. Ed.*, 2023, **62**, 202310033.

17 A. E. Lakraychi, E. Deunf, K. Fahsi, P. Jimenez, J. P. Bonnet, F. Djedaini-Pilard, M. Bécuwe, P. Poizot, and F. Dolhem, *J. Mater. Chem. A.,* 2018, **6**, 19182–19189.

18 Z. Song, Y. Qian, X. Liu, T. Zhang, Y. Zhu, H. Yu, M. Otani, and H. Zhou, *Energy Environ. Sci.,* 2014, **7**, 4077–4086.

19 S. Renault, S. Gottis, A. L. Barrès, M. Courty, O. Chauvet, F. Dolhem, and P. Poizot, *Energy Environ. Sci.,* 2013, **6**, 2124–2133.

20 S. Wang, L. Wang, K. Zhang, Z. Zhu, Z. Tao, and J. Chen, *Nano Lett.*, 2013, **13**, 4404–4409.

21 S. Wang, L. Wang, Z. Zhu, Z. Hu, Q. Zhao, and J. Chen, *Angew. Chemie - Int. Ed.,* 2014, **126**, 6002–6006.

22 L. Sieuw, A. E. Lakraychi, D. Rambabu, K. Robeyns, A. Jouhara, G. Borodi, C. Morari, P. Poizot, and A. Vlad, *Chem. Mater.*, 2020, **32**, 9996–10006.

23 A. Jouhara, N. Dupré, A. C. Gaillot, D. Guyomard, F. Dolhem, and P. Poizot, *Nat. Commun*., 2018, **9**, 4401.

24 D. Rambabu, A. E. Lakraychi, J. Wang, L. Sieuw, D. Gupta, P. Apostol, G. Chanteux, T. Goossens, K. Robeyns, and A. Vlad, *J. Am. Chem. Soc.*, 2021, **143**, 11641–11650.

25 D. L. Williams, J. J. Byrne, and J. S. Driscoll, *J. Electrochem. Soc.,* 1969, **116**, 2.

26 T. Boschi, R. Pappa, G. Pistoia, and M. Tocci, *J. Electroanal. Chem. Interf. Electrochem.,* 1984, **176**, 235-242.

27 Q. Yu, Z. Yao, J. Shi, W. Tang, C. Wang, D. Li, and C. Fan, *Organic Electronics*., 2020, **81**, 105661.

28 T. Takada, M. Arisawa, M. Gyoten, R. Hamada, H. Tohma, and Y. Kita, *J. Org. Chem.,* 1998, **63**, 7698–7706.

29 S. Punna, S. Meunier, and M. G. Finn, *Org. Lett.*, 2004, **6**, 2777–2779.

30 A. Robert, P. Dechambenoit, E. A. Hillard, H. Bock, and F. Durola, *Chem. Commun.,* 2017, **53**, 11540–11543.

31 J. Yang, P. Xiong, Y. Shi, P. Sun, Z. Wang, Z. Chen, and Y. Xu, *Adv. Funct. Mater.*, 2020, **30**, 1–8.

32 S. Bai, B. Kim, C. Kim, O. Tamwattana, H. Park, J. Kim, D. Lee, and K. Kang, *Nat. Nanotechnol*., 2021, **16**, 77–84.

33 T. Yokoji, Y. Kameyama, N. Maruyama, and H. Matsubara, *J. Mater. Chem. A.*, 2016, **4**, 5457-5466.

34 J. E. Almlöf, M. W. Feyereisen, T. H. Jozefiak, and L. L. Miller, *J. Am. Chem. Soc.,* 1990, **112**, 1206–1214.

35 L. Sieuw, A. Jouhara, É. Quarez, C. Auger, J. F. Gohy, P. Poizot, and A. Vlad, *Chem. Sci.*, 2019, **10**, 418–426.

36 J. Multia, J. Heiska, A. Khayyami, and M. Karppinen,. *ACS Appl. Mater. Interfaces*, 2020, **12**, 41557-41566.

37 A. Choi, Y.K. Kim, T.K. Kim, M.S. Kwon, K.T. Lee, and H.R. Moon, *J. Mater. Chem. A.*, 2014, **2**, 14986-14993.

38 J. Asenbauer, T. Eisenmann, M. Kuenzel, A. Kazzazi, Z. Chen, and D. Bresser, *Sustain. Energy Fuels.,* 2020, **4**, 5387–5416.

39 H. Zhang, Y. Yang, D. Ren, L. Wang, and X. He, *Energy Storage Mater.,* 2021, **36**, 147–170.

40

